Current Dynamics over the Northern California Inner Shelf*

STEVEN J. LENTZ

Woods Hole Oceanographic Institution, Woods Hole, Massachusetts

(Manuscript received 12 April 1993, in final form 19 January 1994)

ABSTRACT

Subtidal current dynamics at a northern California inner-shelf site are analyzed using moored current observations in 30 m of water, in conjunction with wind and bottom pressure measurements acquired during the summer of 1981 as part of the first Coastal Ocean Dynamics Experiment. The subtidal flow is driven locally by both an alongshelf wind stress and an alongshelf pressure gradient, which tend to be similar in magnitude but opposite in direction. Model depth-average alongshelf currents are about twice as large as observed. Analyses suggest that this discrepancy is due to a larger drag on the inner-shelf currents than suggested by bottom tripod measurements at the site, due to the presence of large rock outcrops over the inner shelf in this region. A notable characteristic of the observations is the weakness of the alongshelf flow over the inner shelf; alongshelf current standard deviations are a factor of 4 smaller than at midshelf. Analyses suggest this is due to a decrease in the wind stress toward the coast, shallower water resulting in a weaker body force due to the alongshelf pressure gradient and the increased drag on the flow over the inner shelf noted above.

The moored current observations reveal a simple cross-shelf circulation pattern. The near-surface flow was typically offshore in response to equatorward winds with an onshore flow in the lower water column driven by the opposing alongshelf pressure gradient. The depth-average cross-shelf velocity was consistently zero to the accuracy of the observations, suggesting a two-dimensional circulation. A simple two-dimensional eddy viscosity model reproduced the basic features of the observed flow, including the vertical structure, orientation, and temporal variability. The model results showed persistent, substantial vertical stress divergence throughout the water column supporting the notion that the moored observations were at an inner-shelf site where the surface and bottom boundary layers merge.

1. Introduction

The term "inner shelf" has been used in a variety of contexts to refer to the portion of the continental shelf near the coast (Allen et al. 1983). On wind-driven shelves the inner shelf has been defined more explicitly as the region offshore of the surf zone, where the surface and bottom boundary layers interact (Lentz 1993). The direct coupling of the surface and bottom boundary layers results in a cross-shelf divergence of the Ekman transport (Ekman 1905), which can cause coastal upwelling or downwelling (e.g., Smith 1981) and provides the most common forcing mechanism for coastal-trapped waves (e.g., Mitchum and Clarke 1986). Hence, the inner shelf plays a key role in the wind-driven shelf circulation.

The dynamics of inner-shelf currents remain poorly understood, despite its importance to the wind-driven shelf circulation. This is due in part to the lack of observations in this region. The few observational studies of the subtidal (timescales longer than a day) dynamics for this region have tended to focus on the depth-average flow that is principally alongshelf (Pettigrew 1981; Lentz and Winant 1986; Mitchum and Clarke 1986; Masse 1988; and Lee et al. 1989). These studies have generally found that the depth-average alongshelf flow is driven locally by the wind stress and alongshelf pressure gradients and that these two forcing terms are balanced by bottom friction and to a lesser extent accelerations of the alongshelf flow (Pettigrew 1981; Lentz and Winant 1986; and Lee et al. 1989).

Subtidal cross-shelf velocities over the inner shelf are generally weak, a few cm s^{-1}, relative to the accuracy of standard current meters. This problem is aggravated by the need to accurately average the strong surface gravity wave motions, which may extend over the entire water column in this region. Furthermore, the vertical structure of the inner-shelf circulation has generally not been well resolved since most moored observations have consisted of only a few current meters spanning the vertical. Previous studies have found that, while the depth-averaged cross-shelf velocity $\langle u \rangle$ is usually small relative to the accuracy of the estimate, the associated Coriolis force ($f\langle u \rangle$, where f is the Coriolis frequency) is often relatively large but uncorrelated with other terms in the alongshelf momentum balance (Pettigrew 1981; Lentz and Winant 1986; and

---

* Contribution Number 8308.

Corresponding author address: Dr. Steven J. Lentz, Woods Hole Oceanographic Institution, Woods Hole, MA 02543.

Lee et al. 1989). This has led to speculation that either there were unresolved alongshelf pressure gradients (Pettigrew 1981) or estimates of $\langle u \rangle$ were unreliable due to the problems cited above (Lentz and Winant 1986). This is an important issue since it bears on whether the inner-shelf circulation is essentially two-dimensional (variations in the vertical and cross-shelf directions), a fundamental assumption in many models of the inner-shelf circulation (e.g., Mitchum and Clarke 1986; Lentz 1993).

To gain insight into the characteristics and dynamics of subtidal currents over the inner shelf, observations from a single mooring site located in 30 m of water are analyzed. The mooring site (designated C1) was part of the first Coastal Ocean Dynamics Experiment (CODE-1) moored array deployed over the northern California shelf during the summer of 1981. The C1 observations provide several elements lacking in most previous inner-shelf observations. There were five vector-measuring current meters (VMCM) spanning the water column providing relatively good vertical coverage with instruments designed to make accurate current measurements in the presence of waves (Weller and Davis 1980). CODE-1 also included an array of bottom pressure sensors for estimating the pressure gradient field (Brown et al. 1987). While there has been considerable analysis of the CODE current observations (Lentz 1990), the observations from the C1 mooring have received little attention.

A brief overview of the CODE-1 field program focusing on the C1 mooring site and a discussion of the estimation of the local forcing, wind stress, and alongshelf pressure gradient are given in section 2. A simple eddy viscosity model used to aid in interpreting the observations is also described in section 2 and in the appendix. The basic characteristics of the subtidal current and temperature observations from the C1 mooring site are presented in section 3. The dynamics of the depth-average and depth-dependent components of the flow are examined in sections 4 and 5, respectively. Results are summarized in section 6.

2. Background

a. *Study site and methods*

The CODE-1 field program took place on the northern California shelf from April through July 1981. The central line of the CODE-1 moored array, which included the C1 mooring site, was located between Point Reyes and Point Arena (Fig. 1). The shelf at this location is about 15 km wide with a relatively steep bottom slope (3.5×10^{-2}) from the coast to the 70-m isobath and a more gradual bottom slope (0.5×10^{-2}) from the 70-m isobath to the shelf break. The C1 site was located on the 30-m isobath approximately 0.7 km offshore in the region of steep bottom slope. The local isobath orientation at the C1 mooring site is ~335° T over scales of a few kilometers (Fig. 1). Consequently, a right-handed coordinate system is adopted with alongshelf positive toward 335° T and cross-shelf positive toward 65° T. This is different from the standard CODE coordinate system in which alongshelf is defined as 317° T (Winant et al. 1987).

Two moorings were deployed at the C1 site. A surface mooring with VMCMs at depths 4, 7, 11, and 14 m and a subsurface mooring supporting VMCMs at depths 23 and 27 m. The VMCM at 14-m depth returned no data. The other five VMCMs returned complete records with a common time period for this study of 4 April–21 July 1981. The VMCMs are believed to measure currents with an accuracy of 1–2 cm s^{-1} in the presence of surface gravity waves (Weller and Davis 1980).

This study will focus on subtidal variability having timescales longer than a day. Consequently, the time series presented have been low-pass filtered to suppress tidal and higher frequency motions using PL64 (Rosenfeld 1983). Because of the large tidal peaks in the bottom pressure data (discussed below), the major tidal components were removed using a least-squares analysis prior to low-pass filtering.

b. *Local forcing*

The relationships between the C1 current observations and the local wind stress and alongshelf pressure gradient are discussed in sections 4 and 5. The procedures used to estimate time series of the wind stress and alongshelf pressure gradient are presented below.

1) WIND STRESS

An anemometer mounted on the C1 surface buoy failed. Consequently, no wind data were acquired at the C1 mooring site. The closest two wind stations to the C1 site were a coastal station at Sea Ranch, about 2 km north of the C1 mooring, and the C3 meteorological buoy, approximately 7 km offshore from the C1 mooring (Fig. 1). The C3 observations are used to represent the wind at the C1 mooring, because the coastal topography strongly influenced the characteristics of the winds at Sea Ranch (Fig. 2). In general, wind stress (estimated following Large and Pond 1981) is well correlated over the CODE region (Lentz and Chapman 1989). However, observations from both CODE-1 and CODE-2 indicate there were large gradients in the wind stress magnitude near the coast (Fig. 3). Over the middle and outer shelf the major-axes standard deviations of wind stress tend to be relatively uniform, typically about 1 dyn cm^{-2}. The major-axes standard deviations of coastal wind stresses are about 0.5 dyn cm^{-2} or less. Mean wind stresses exhibit a similar pattern. Consequently, the magnitude of the wind stress at C1 is uncertain. The C1 wind stress was estimated

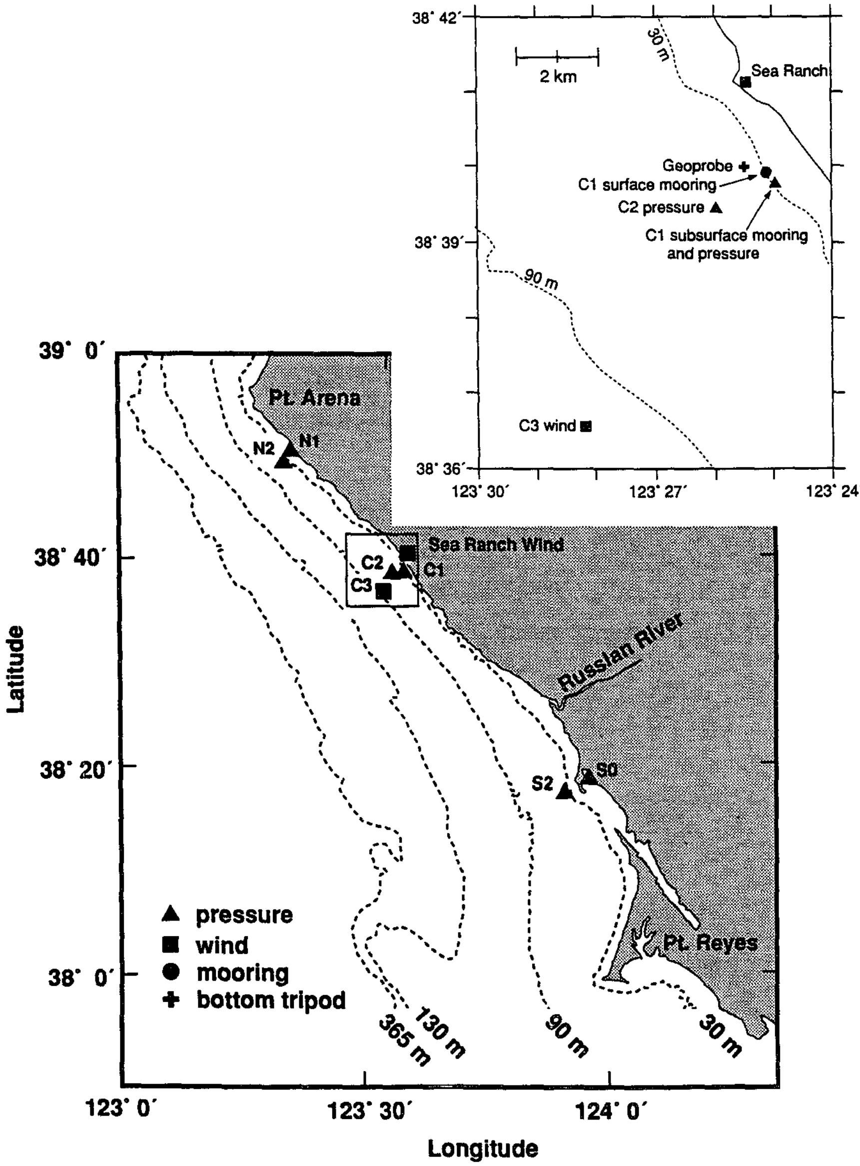

FIG. 1. Map of the northern California shelf showing the locations of the CODE-1 instrument sites discussed in this study, including a blowup of the area around the C1 site. GEOPROBE is a bottom tripod discussed in section 4.

by multiplying the C3 wind stress by one third. This choice is based on the simplest possible cross-shelf structure to the wind stress variability that is consistent with the observations presented in Fig. 3: the wind stress standard deviations decrease linearly between C3 and Sea Ranch. Because of the uncertainty in the correct magnitude of the C1 wind stress other choices are considered in section 4. Analyses presented in section 4 suggest the choice of one-third is most consistent with the current observations at C1. The major axis of the wind stress is also assumed to be aligned with the coastline near C1. This assumption is based on the proximity of C1 to the coast and the presence of the coastal mountains (Fig. 2). In general, results presented are not very sensitive to the precise orientation of the wind stress. A decrease in the wind stress magnitude near the coast and an orientation parallel to the coast are qualitatively consistent with recent modeling studies of the marine boundary layer for this region (Samelson 1992). However, while such modeling efforts have provided considerable insight into the marine boundary layer dynamics (see also Winant et al. 1988), the models are too idealized to provide more guidance into the detailed cross-shelf structure of the wind stress over the inner shelf.

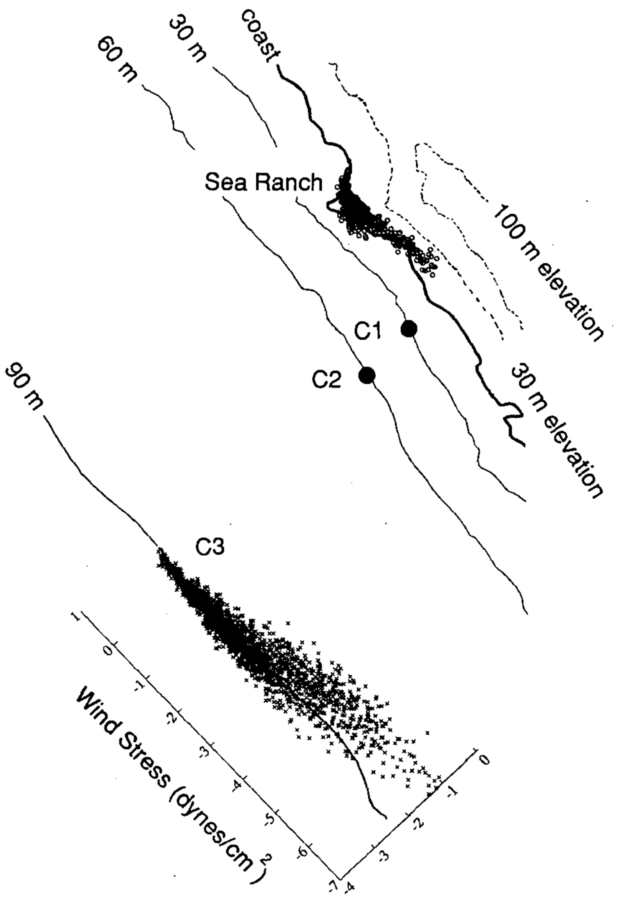

FIG. 2. Scatterplots of the winds at Sea Ranch and C3 showing the topographic influence on the winds at Sea Ranch.

2) ALONGSHELF PRESSURE GRADIENT

CODE-1 included an array of bottom pressure sensors for estimating the pressure gradient field (Brown et al. 1987). As part of this array, six bottom pressure sensors were deployed over the inner portion of the shelf (Fig. 1): three along the 60-m isobath (N2, C2, and S2); two on the 30-m isobath (N1 and C1); and one in 4 m of water inside Bodega Bay Harbor (S0). Estimates of the alongshelf pressure gradient from individual sensor pairs may be inaccurate due to instrument noise and unresolved spatial variability. Additionally, slight variations in the relative cross-shelf location of the sensors may result in the much larger cross-shelf pressure gradient contaminating estimates of the alongshelf pressure gradient. To reduce these problems, an empirical orthogonal function (EOF) analysis of the six inner-shelf bottom pressure records was used to determine the coherent spatial structures of the bottom pressure field resolved by the observations. [The EOFs presented in this study are the eigenfunctions of the covariance matrix of observations or model results, e.g., Davis (1976).] The largest EOF accounted for 96.4% of the variance, while the second EOF accounted for 2% of the variance. However, almost all of the alongshelf pressure gradient variance was contained in the second EOF (Fig. 4). Consequently, the alongshelf pressure gradient was estimated by multiplying the second EOF time series by a least-squares estimate of the slope of the second EOF amplitudes as a function of alongshelf distance. The resulting estimate of the alongshelf pressure gradient is consistent with estimates based on individual bottom pressure sensor pairs. The alongshelf pressure gradient is assumed to be vertically uniform. Estimates based

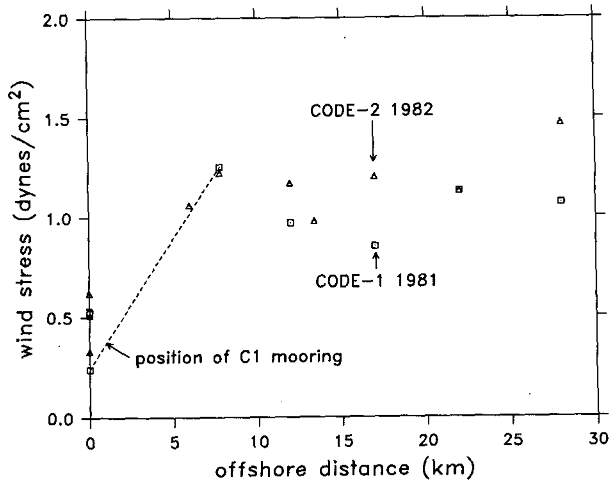

FIG. 3. Major-axis standard deviations of wind stress for CODE-1 and CODE-2 wind stations vs offshore distance. The C1 wind stress was estimated from the C3 wind stress by assuming the wind stress magnitude decreased linearly to the value at the coast (Sea Ranch).

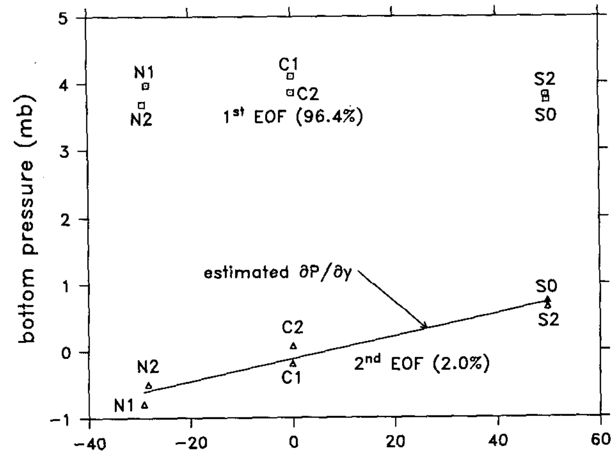

FIG. 4. Structure of the largest two EOFs of bottom pressure from six CODE-1 inner-shelf stations as a function of alongshelf position. A time series of the alongshelf pressure gradient was estimated by multiplying the time series for the second EOF by the slope of the line labeled $\partial P/\partial y$.

TABLE 1. Statistics of the subtidal cross-shelf and alongshelf currents for the period 0000 UTC 4 April–0000 UTC 21 July 1981. Units are centimeters per second.

	Cross-shelf current		Alongshelf current	
Depth (m)	Mean	Std dev	Mean	Std dev
4	−1.5	1.7	−3.6	5.9
7	0.1	0.8	−0.2	5.3
11	1.2	0.9	1.4	5.1
23	1.0	0.9	0.6	5.4
27	0.3	1.0	0.8	4.3
Depth average	0.4	0.5	0.0	5.0

on temperature observations during CODE-1 and during the 1982 CODE-2 field program indicate that this is a good assumption for the inner shelf.

The absolute bottom pressures are not known well enough to estimate the time-averaged alongshelf pressure gradient. Drift of the bottom pressure sensors also makes trends in the estimated alongshelf pressure gradient unreliable (Brown et al. 1987). While the focus of this study is on the subtidal variability, the absolute alongshelf pressure gradient, including the mean, is needed for the model runs discussed below. Consequently, the alongshelf pressure gradient time series is detrended, and the mean alongshelf pressure gradient is estimated by assuming it balances the mean alongshelf wind stress in the depth-average alongshelf momentum balance. The justification for this assumption is discussed in detail in section 4. The subtidal variability of the model results is not very sensitive to the exact choice of the mean alongshelf pressure gradient.

c. *Model*

A simple two-dimensional, eddy viscosity model is used to aid in interpreting the C1 current observations. The model is similar to the one used by Lentz (1993). The momentum balance, neglecting the nonlinear advective terms, is

$$\frac{\partial \mathbf{v}}{\partial t} + f\mathbf{k} \times \mathbf{v} = -\frac{\nabla P}{\rho_0} + \frac{\partial}{\partial z}\left(A_v \frac{\partial \mathbf{v}}{\partial z}\right), \qquad (1)$$

where $\mathbf{v}$ is the velocity vector, f is the Coriolis parameter, ∇ is the horizontal gradient operator, P is pressure, ρ_0 is a reference density, and $A_v(z)$ is the eddy viscosity. A coordinate system is adopted in which x is the cross-shelf coordinate (positive onshore), y is the alongshelf coordinate (positive poleward), and z is the vertical coordinate (positive upward). Boundary conditions for (1) are

$$A_v \frac{\partial \mathbf{v}}{\partial z} = \frac{\tau^S}{\rho_0} \quad \text{at} \quad z = z_{0S} \qquad (2)$$

and

$$\mathbf{v} = 0 \quad \text{at} \quad z = -D + z_{0B}, \qquad (3)$$

where τ^S is the wind stress vector, z_{0S} and z_{0B} are surface and bottom roughness, and D is the water depth. The flow is assumed to be two-dimensional (i.e., $\partial \mathbf{v}/\partial y = 0$). This assumption combined with the constraint of no flow through the coast and continuity requires that

$$U = \int_{-D}^{0} u dz = 0 \qquad (4)$$

everywhere. With the assumption that the flow is two-dimensional, (1) is forced locally by the wind stress τ^S and the alongshelf pressure gradient $\partial P/\partial y$.

Given time series of the forcing terms, τ^S and $\partial P/\partial y$ and a prescription for the eddy viscosity profile $A(z)$, Eq. (1) subject to (2)–(4) is solved for the velocity profile $\mathbf{v}(z)$ and the cross-shelf pressure gradient $\partial P/\partial x$ using a numerical procedure outlined in Patankar (1980). The model implementation is described in the appendix. Note that the model is essentially one-dimensional except for the constraint that there is no net cross-shelf transport (4). The cross-shelf pressure gradient $\partial P/\partial x$ is found that satisfies this constraint. The model estimates of $\partial P/\partial x$ are in geostrophic balance with the midwater column alongshelf current estimates, as expected from midshelf observations (Brown et al. 1987). Consequently, comparisons between the model and observations in the following section will focus on the currents.

Four different forms for the eddy viscosity profile $A(z)$ are examined because Lentz (1993) has shown that for the inner-shelf region some results from this model are sensitive to the form of the eddy viscosity. The eddy viscosity profiles chosen depend only on the surface and bottom stresses and distance from the boundaries. In particular, it is assumed that stratification does not influence variability in the eddy viscosity profile. This assumption is based on the observation that the vertical temperature gradient was usually weak at the C1 mooring (Fig. 5) and is motivated by a desire to find the simplest model that represents the basic characteristics of the observations. Descriptions of the different eddy viscosity profiles considered are included in the appendix.

Besides the forcing terms and the form of the eddy viscosity profile, the standard model inputs were the water depth (D = 30 m), Coriolis frequency $f = 0.909 \times 10^{-4}\ \mathrm{s}^{-1}$, and effective bottom roughness z_{0B} = 1 cm. The choice for the effective bottom roughness was based on results from a bottom tripod deployed less than 1 km from the C1 mooring (Fig. 1) from 3 to 15 June 1981 (Drake et al. 1992) and included the influence of surface gravity waves on the bottom stress. Results are not sensitive to the choice of z_{0S} (Lentz 1993), which was also set equal to 1 cm.

3. Current observations

The subtidal C1 currents are polarized, with alongshelf current standard deviations 3.5–6.5 times larger than cross-shelf current standard deviations (Table 1). Alongshelf currents are characterized by events lasting days to weeks with current magnitudes of 5–10 cm s^{-1} (Fig. 5). Alongshelf currents at 4-m depth are generally equatorward, consistent with the wind stress. Alongshelf currents at 7 m and below are fairly uniform with depth and are more often poleward. Consequently, currents at 4-m depth were often in the opposite direction to the currents at 7-m depth and below, most notably in late May to early June and mid-July.

A striking characteristic of the C1 observations is how weak the subtidal currents are relative to midshelf currents (Fig. 6). There is a factor of 4 decrease in the depth-average alongshelf-current standard deviations from the midshelf C3 site to C1, with much of the decrease occurring close to the coast between C2 and C1. This decrease toward the coast in subtidal current standard deviations over the inner half of the shelf was a general feature of the CODE current observations (Winant et al. 1987; Kosro 1987) and has also been observed on other shelves (e.g., Lentz and Winant 1986; Lee et al. 1989).

Water temperatures are typically between 7° and 9°C with a temperature difference of only a few tenths of a degree across the water column (Fig. 5). The one notable exception to this is a weeklong period in early July when the winds are weak, water temperatures exceed 11°C, and the temperature difference across the water column is over 1°C. This response to periods of weak winds (wind relaxations) during CODE was ex-

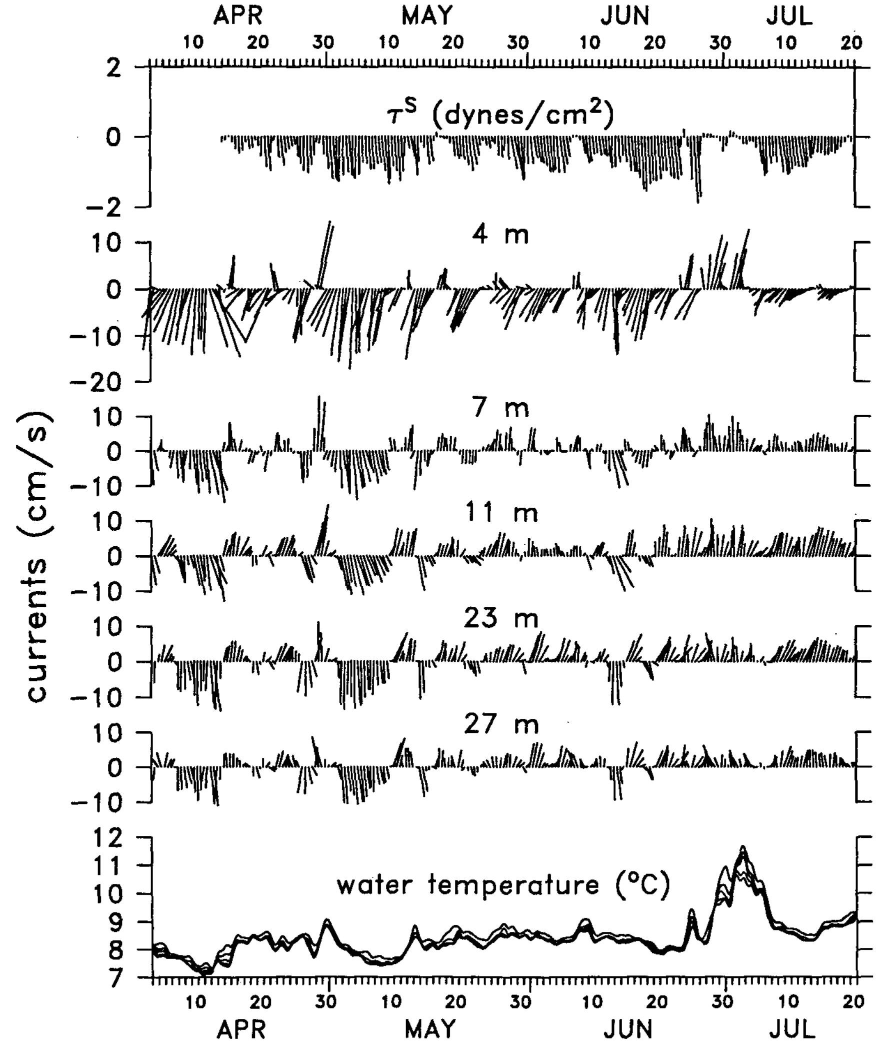

FIG. 5. Vector time series of the low-pass filtered wind stress currents at depths 4, 7, 11, 23, and 27 m on the C1 mooring and the water temperature at these depths. Vectors pointing toward the top of the figure are oriented alongshelf, toward 335° T, with onshore toward the right.

amined by Send et al. (1987). From mid-April to late June there is a fairly constant temperature difference of ~0.3°C at depths between 4 and 7 m with relatively uniform temperatures between 7 and 27 m.

The cross-shelf current observations reveal a simple circulation pattern (Fig. 7). At 4-m depth there is an offshore current of 2–4 $\mathrm{cm\ s^{-1}}$ during equatorward winds with short bursts of onshore flow during periods of weak winds. At 7-m depth, only 3 m deeper, the cross-shelf current is very weak, typically less than 1 $\mathrm{cm\ s^{-1}}$, with no preferred on/offshore direction. At 11, 23, and 27 m the cross-shelf current is generally onshore at 1–2 $\mathrm{cm\ s^{-1}}$. The mean cross-shelf current is 1.5 $\mathrm{cm\ s^{-1}}$ offshore at 4-m depth and ~1.0 $\mathrm{cm\ s^{-1}}$ onshore over the lower water column (Table 1). These cross-shelf flows are at the accuracy limits of the VMCMs (Weller and Davis 1980); however, the consistency of the circulation pattern, the tendency of the depth-average cross-shelf flow to be nearly zero (discussed below), and the model results (section 5) all suggest that the observed cross-shelf flow is not simply instrument noise. While this cross-shelf circulation is relatively weak, it is still a very effective mechanism for cross-shelf exchange, because the volume of water between the coast and the 30-m isobath is small. The mean cross-shelf circulation (Table 1) can replace the water inshore of the 30-m isobath in about a day.

The cross-shelf currents in Fig. 7 suggest a tendency for the near-surface offshore transport to be balanced by an onshore transport in the lower water column. To quantify this tendency the vertically averaged cross-shelf current was estimated by taking the sum of the five current measurements each weighted by the fraction of the water column associated with each current meter. The resulting depth-average cross-shelf current magnitudes rarely exceed 1 $\mathrm{cm\ s^{-1}}$ (bottom of Fig. 7) and the mean and standard deviation are generally smaller than at individual current meters (Table 1). This is well within the measurement accuracy of the VMCMs (Weller and Davis 1980) and the uncertainties in the vertical average due to the coarse vertical resolution. Thus, to the accuracy of the measurements, the transport at C1 during CODE-1 was alongshelf on timescales from days to months, consistent with a two-dimensional subtidal circulation.

The vertical structure of the currents at C1 may be summarized by two EOFs, which account for 97% of the total current variance (Fig. 8). In the EOF analysis the cross-shelf and alongshelf currents are input separately as scalars. An EOF analysis of the current vectors as complex variables yields the same results because the largest two EOFs tend to be rectilinear.

The largest EOF accounts for 89.2% of the total current variance and is oriented roughly alongshelf. Variations from an alongshelf orientation are 5° or less for the individual current meters. The time series associated with this EOF is essentially identical to the depth-average alongshelf current; the correlation is 0.998, and the regression coefficient is 1.00. The largest EOF accounts for 12% of the total subtidal cross-shelf current variance and 92% of the alongshelf current variance. It is uncertain whether cross-shelf currents in this EOF represent a real signal or are associated with orientation uncertainties in the current observations. This question is discussed in section 5.

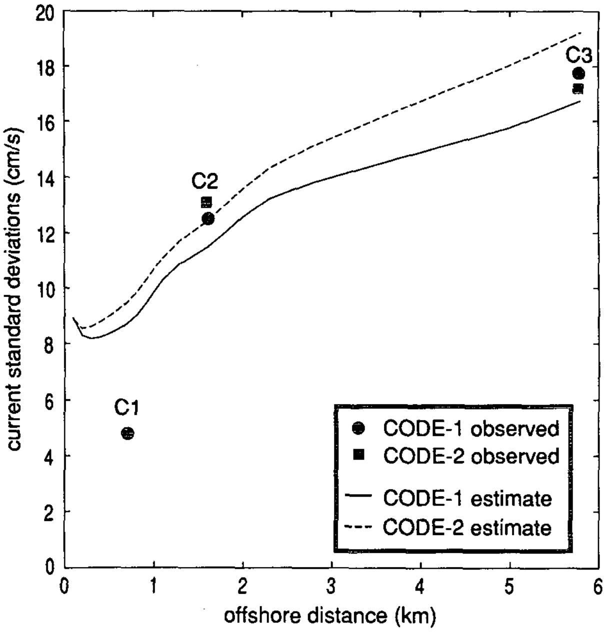

FIG. 6. The standard deviation of the depth-average alongshelf current as a function of offshore distance from the CODE observations (symbols). The cross-shelf variation of depth-average alongshelf velocity standard deviations due to the decrease in wind stress and water depth toward the coast estimated by integrating (5) is also shown (solid and dashed lines). The procedure for making these estimates and the results are discussed in section 4c.

The second EOF accounts for 7.7% of the total variance and is oriented approximately 30° clockwise relative to the local isobaths, with flow in opposite directions in the upper and lower portions of the water column. The change in orientation of the flow occurs at about 11-m depth. The second EOF accounts for 47% of the total subtidal cross-shelf variance and 6% of the alongshelf current variance.

The C1 current observations suggest that the flow may be decomposed into two components, a depth-averaged alongshelf current and a depth-dependent current. The dynamics of these two components are examined in the following sections. Of particular interest are two questions: Why is the depth-average alongshelf flow at C1 so much weaker than the midshelf flow and what determines the vertical structure and orientation of the depth-dependent flow?

4. Depth-average flow

a. Dynamics

The linear, depth-average, alongshelf momentum balance is

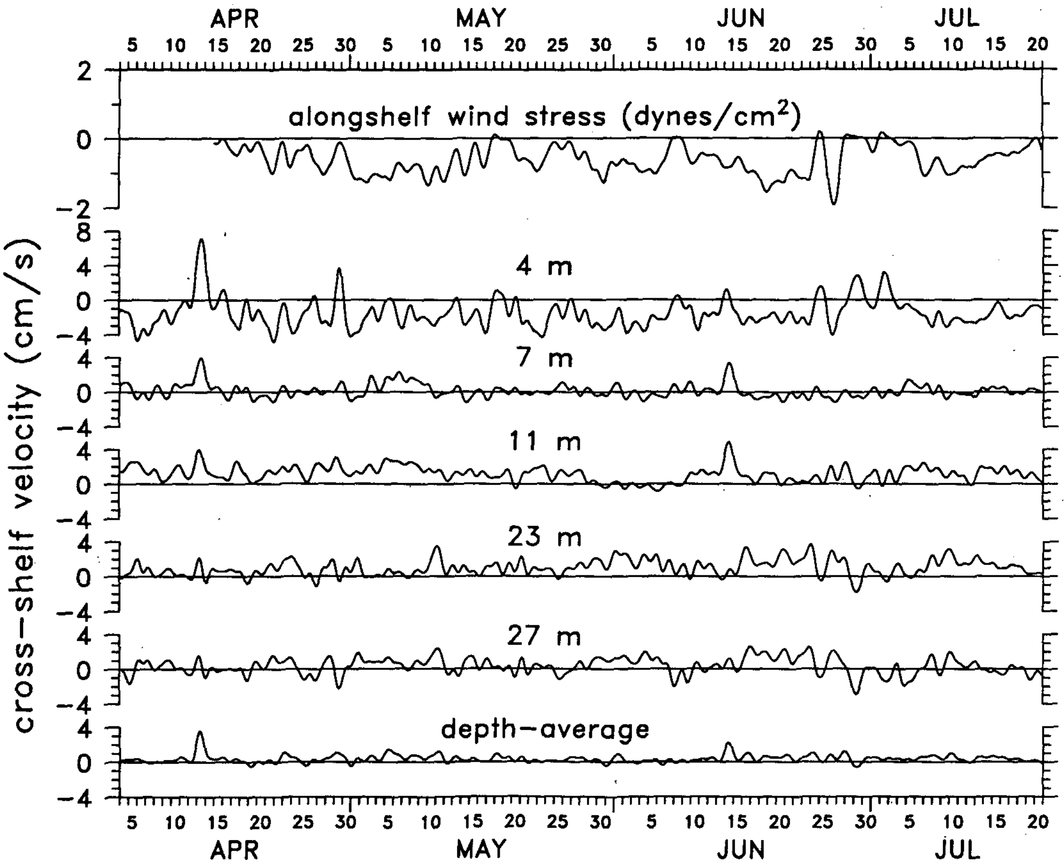

FIG. 7. Time series of the alongshelf wind stress and cross-shelf currents at 4, 7, 11, 23, and 27 m on the C1 mooring and the estimated depth-average cross-shelf current. Positive winds are poleward and positive currents are onshore.

$$\frac{\partial\langle v\rangle}{\partial t}+f\langle u\rangle=-\frac{1}{\rho_0}\frac{\partial P}{\partial y}+\frac{\tau^{Sy}}{\rho_0 D}-\frac{\tau^{By}}{\rho_0 D},\qquad(5)$$

where $\langle u\rangle$ and $\langle v\rangle$ are the depth-average cross-shelf and alongshelf velocities, and τ^{Sy} and τ^{By} are the alongshelf components of wind stress and bottom stress. As discussed in section 2b, the alongshelf pressure gradient is assumed to be independent of depth. All terms in (5) may be estimated from the available observations given a drag coefficient C_D relating the bottom stress to the flow at some depth. Observations from a bottom tripod deployed less than 1 km from the C1 mooring (Fig. 1) from 3 to 15 June 1981 (Drake et al. 1992) yielded estimates of the effective bottom roughness z_0 of about 1 cm, including the influence of surface gravity waves. These estimates were made by fitting the observed current speeds to a logarithmic profile and estimating z_0 from the intercept. The corresponding C_D 3 m above the bottom is about 5×10^{-3}. The bottom stress is estimated using the current observations from the 27-m VMCM as

$$\tau^B=\rho_0 C_D\mathbf{v}|\mathbf{v}|.\qquad(6)$$

Means and standard deviations of the estimated terms in (5) are listed in Table 2. The time-average alongshelf pressure gradient cannot be determined from the pressure observations. However, the mean alongshelf wind stress is nearly an order of magnitude larger than the other three terms in (5), suggesting that it is balanced by a mean alongshelf pressure gradient. This result is robust to the details of the bottom stress formulation, since the mean wind stress is two orders of magnitude larger than the estimated bottom stress. Even a factor of 10 change in C_D would not make the bottom stress large enough to substantially change the presumed mean balance between the wind stress and an alongshelf pressure gradient. The estimated mean alongshelf pressure gradient has the same sign (sea level rising to the south), but is a factor of 2 or more larger than large-scale estimates of the average alongshelf pressure gradient during spring and summer in this region based on historical data (e.g., Hickey and Pola 1983). The discrepancy in magnitude is not surprising given that the historical data is typically based on station separations of several hundred kilometers and represent a long-term average.

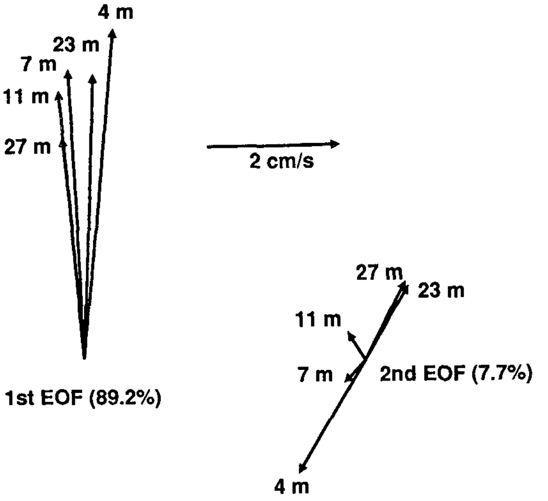

FIG. 8. Plan view of the largest two EOFs for the observed C1 currents. Each vector corresponds to a particular current meter, the depth of which is noted at the end of the vector. Vectors oriented vertically correspond to alongshelf current variability.

TABLE 2. Statistics of terms in the depth-average alongshelf momentum balance (5), for the period 0000 UTC 4 April–0000 UTC 21 July 1981. Units are 10^{-4} cm s^{-2}.

	$\frac{\partial v}{\partial t}$	fu	$\frac{1}{\rho_0}\frac{\partial P}{\partial y}$	$\frac{\tau^{Sy}}{\rho_0 D}$	$\frac{\tau^{By}}{\rho_0 D}$
Mean	0.0	0.3	—	−2.2	0.0
Standard deviation	0.7	0.4	1.4	1.4	0.5

Subtidal fluctuations in τ^{Sy}/D and $\partial P/\partial y$ have roughly the same magnitude but opposite signs at C1 (Fig. 9) and are larger than the other terms in (5) (Table 2). During the latter half of the CODE-1 deployment (June–early July) there is a clear correspondence between fluctuations of the alongshelf wind stress and the alongshelf pressure gradient with the wind stress leading by about half a day. This indicates that an alongshelf pressure gradient is set up that opposes the wind stress. In contrast, during the first half of the deployment (late April–May) there is not such an obvious correspondence between the alongshelf wind stress and the alongshelf pressure gradient. It is unclear what causes this change in the relationship between the alongshelf wind stress and the alongshelf pressure gradient. Examination of coastal wind observations to the south (the direction from which coastal-trapped waves may propagate into the region) does not reveal any obvious change in the wind stress pattern between the first and second halves of the C1 deployment. Observations from other inner shelves suggest that in some cases $\partial P/\partial y$ tends to oppose τ^{Sy} (Pettigrew 1981; Masse 1988), while in other cases they are uncorrelated (Lentz and Winant 1986; Lee et al. 1989).

The combination of the alongshelf wind stress and pressure gradient forcing should be balanced by accelerations of the depth-average alongshelf flow and the alongshelf component of the bottom stress, if the Coriolis force associated with the depth-average cross-shelf flow and the nonlinear terms are small. This response is evident in comparing the observed depth-average alongshelf current and the two local forcing terms in Fig. 9. (Note that a negative $\partial P/\partial y$ drives a positive alongshelf current.) When the wind stress is much stronger than the alongshelf pressure gradient, as in early May, the depth-average alongshelf flow is equatorward. However, in the latter half of June, when the two forcing terms are about equal, the depth-average alongshelf flow fluctuates between poleward and equatorward events depending on the relative strength of the two forcing terms.

To make a more quantitative comparison, the model described in section 2c and appendix A was run assuming a bottom roughness of 1 cm (Drake et al. 1992). For comparison, (5) was also integrated directly assuming $\langle u \rangle = 0$ and $\tau^{By} = r\langle v \rangle$, where $r = 0.05$ cm s^{-1} is a linear drag coefficient. In the context of the

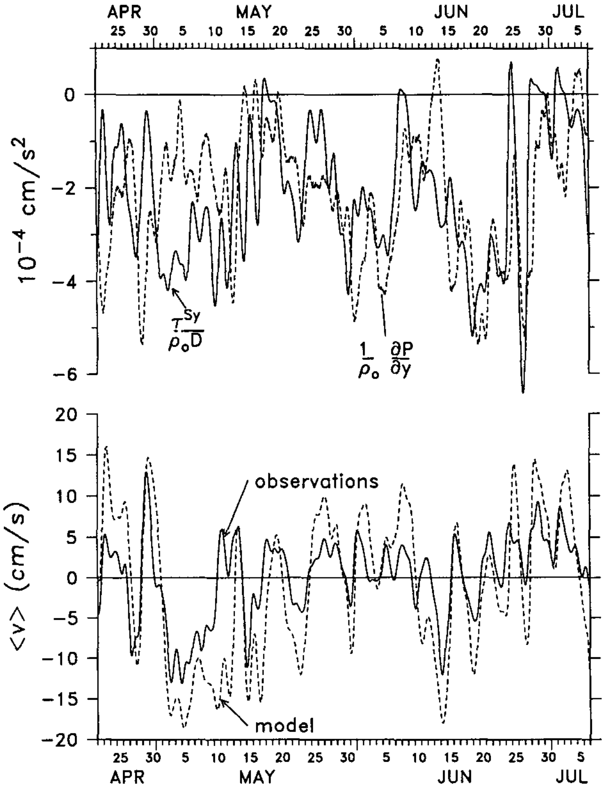

FIG. 9. Time series of the estimates of alongshelf wind stress and pressure gradient forcing (upper panel) and depth-average alongshelf velocity $\langle v \rangle$ from the observations and model. Correlation between the observed and model $\langle v \rangle$ is 0.8. The particular model results shown are from the numerical model using the exponential eddy viscosity profile. However, model results using the other eddy viscosity profiles or integrating (5) yield essentially identical time series of $\langle v \rangle$.

depth-average flow these two approaches are nearly identical except in the prescription of the bottom stress. The resulting time series from these two models are essentially the same, correlation 0.98 and regression coefficient of 1.1.

The model results agree well with the observed depth-average alongshelf velocity (Fig. 9); correlations are 0.81 for estimates based on integrating (5) and 0.80 for estimates from the numerical model, independent of the form of the eddy viscosity. However, the magnitude of the model depth-averaged alongshelf flow in all cases is about twice as large as the observed depth-average alongshelf flow.

To determine the generality of this discrepancy, the depth-average flow at the C2 site during CODE-2 was also compared to model estimates. There were four current meters at depths of 10, 20, 35, and 53 m in 60 m of water at the CODE-2 C2 site. Model runs were made using the CODE-2 C3 wind stress and an alongshelf pressure gradient estimated from the N2, C2, and R2 bottom pressure measurements (Brown et al. 1987) in the manner described in section 2b. The resulting depth-average alongshelf currents at C2 from the observations and model results are well correlated (correlation 0.83) and similar in magnitude (standard deviations 13.6 and 15.8 cm s^{-1}, respectively; regression coefficient 0.96). Thus, the discrepancy in amplitude at C1 during CODE-1 is not evident at C2 during CODE-2. Possible explanations for the discrepancy at C1 are discussed in the next section.

b. Magnitude of depth-averaged flow

Three possible explanations for the discrepancy in amplitude between the observed and model depth-averaged flows are considered: the prescribed forcing is too large; tidal and higher frequency variability not included in the model may result in a larger bottom stress; and the drag on the flow is larger than expected from the tripod measurements, possibly due to large rock outcrops in the region.

There is no obvious reason to suspect the magnitude of the alongshelf pressure gradient. However, as noted in section 2b, the magnitude of the wind stress is less certain. Therefore, model calculations were repeated with a wind stress magnitude that was half the standard value. This choice reduces the wind stress standard deviation to slightly less than the coastal value at Sea Ranch, which is presumably a lower bound. This resulted in only a small (10%) decrease in the amplitude of the depth-average flow from the model, suggesting that the discrepancy is not due to choosing too large an amplitude for the C1 wind stress. Furthermore, the correlation between the depth-average alongshelf flow for the model results and observations decreased significantly from 0.79 to 0.65. Doubling the standard wind stress to two-thirds the C3 wind stress also resulted in a decrease in the correlation to 0.70, supporting the notion that the wind stress magnitude at C1 is about one-third the C3 wind stress magnitude.

The model does not include tidal and higher frequency variability, which contribute to the bottom stress and thus will result in an effectively larger drag coefficient on the lower-frequency flow. Since the tidal-band variance at C1 tends to be smaller than the subtidal variance, the bottom stress should be dominated by the subtidal variability. Nevertheless, to determine whether the neglect of tidal and higher-frequency variability could account for the difference in amplitude between the model results and the observations, the model was forced with the unfiltered wind stress, which includes a strong diurnal component, and a semidiurnal fluctuation was added to the alongshelf pressure gradient time series. The magnitude of the semidiurnal pressure gradient was chosen so that the resulting semidiurnal tidal currents are slightly larger than those observed (peak tidal currents of order 5 cm s^{-1}). No attempt was made to represent the details of the observed tidal variability realistically since the amplitude of the tidal currents was assumed to be the primary factor influencing bottom stress on the subtidal flow. The resulting model currents were low-pass filtered in the same way as the observations. Inclusion of the tidal variability resulted only in a slight (<5%) decrease in the model depth-average alongshelf flow.

Another possibility is that the drag on the flow may be larger than indicated by the bottom tripod measurements. Side-scan sonar measurements in the region reveal a very rough bottom over the inner shelf with rock ledges and irregular rock outcrops (Cacchione et al. 1983). Cacchione et al. (1983) note that while "no rocky features were found within 0.5 km of C1 (GEOPROBE site Fig. 1), farther north and south many striking hard rock outcrops cover the seafloor." Prominent rock outcrops were also visible extending out of the water nearer shore. It seems plausible, if not likely, that these features exert a significant drag on the inner-shelf flow. This drag on the flow may be independent of the bottom roughness and stress estimates from the GEOPROBE tripod, which focuses on the local adjustment of the near-bottom flow. While it is unclear how to represent intermittent rock outcrops (e.g., Smith and McClean 1977), model runs indicate that a bottom roughness of 10 cm yields model depth-averaged current magnitudes that match the observations. This order of magnitude increase in z_0 changes the amplitude of the depth-averaged alongshelf current variability, without substantially altering the temporal characteristics of the depth-averaged flow (or the vertical structure of the largest two EOFs discussed in section 5). Cacchione et al. (1983) note that the rock outcrops can be several meters in elevation, which is crudely consistent with $z_0 = 10$ cm, assuming that $z_0 = d/30$ for a turbulent boundary layer, where d is the physical height of roughness elements (Schlichting 1979). Finally, since the rock outcrops were only observed inshore of the 60-m isobath (Cacchione et al. 1983), this explanation is consistent with the result that there is no discrepancy between depth-averaged alongshelf currents from the observations and model results at the CODE-2 C2 mooring in 60 m of water. Thus, the most plausible explanation for the discrepancy in the magnitudes of the observed and modeled depth-averaged alongshelf flows is that large rock outcrops over the inner shelf in this region impose a significant drag on the flow.

c. *Cross-shelf structure*

The magnitude of alongshelf current fluctuations decreases substantially from midshelf (C3) to the C1 mooring site (Fig. 6). Examination of (5) suggests that cross-shelf variations in the wind stress, alongshelf pressure gradient, water depth, and bottom stress may all contribute to this decrease. The alongshelf wind stress decreases by a factor of 3 or more between midshelf and the coast (Fig. 3). Comparison of separate estimates of $\partial P/\partial y$ during CODE-1 along the 60-m and 30-m isobaths indicates little cross-shelf variation over the inner shelf. However, it is unknown how much variation in $\partial P/\partial y$ occurs between the 60-m and 90-m isobaths. It is also unknown how much cross-shelf variation there is in the bottom stress or C_D. Tripod measurements from a midshelf site (C3), water depth 90 m, (Grant et al. 1984) and from the inner shelf GEOPROBE site, water depth 35 m, (Drake et al. 1992), both in early June 1981 (though not simultaneous), yielded similar estimates for bottom stress ($u_* = 0.3 - 1$ cm s^{-1}) and the 1-m bottom drag coefficient ($C_D = 5 - 10 \times 10^{-3}$). However, this data represents relatively few estimates, 15 profiles at the 90-m site and 19 profiles at the 35-m site, making it tenuous to generalize. Furthermore, as noted above, the drag over the inner portion of the shelf may be larger than suggested by the tripod estimates due to the presence of large rock outcrops. In contrast the bottom is relatively featureless at midshelf in this region (Grant et al. 1984).

To determine how much of the decrease in the alongshelf current variability between C3 and C1 could be accounted for by the decrease in wind stress and water depth alone, the depth-average alongshelf velocity was estimated from (5) for various offshore locations from nearshore to midshelf. Estimates were made for both CODE-1 and CODE-2. The CODE-2 alongshelf pressure gradient was estimated from three bottom pressure sensors along the 60-m isobath using the same procedure outlined in section 2b. The C3 wind stress during CODE-1 and CODE-2 was assumed to decrease linearly from C3 to C1 with the C1 magnitude being a third of the C3 wind stress. Bottom stress was estimated assuming a constant linear drag coefficient $r = 0.05$ cm s^{-1} that did not vary with distance offshore. As noted previously, the numerical eddy viscosity model gives essentially identical estimates for the depth-average alongshelf flow. Standard deviations of the resulting depth-average alongshelf velocity as a function of distance offshore for both CODE-1 and CODE-2 are shown in Fig. 6. The model standard deviations suggest that the decrease in the wind stress and water depth can account for all the observed decrease between C3 and C2 but only about half the observed decrease between C2 and C1. The larger observed decrease between C2 and C1 is probably not due to cross-shelf variations in $\partial P/\partial y$ since $\partial P/\partial y$ was about the same along the 60-m and 30-m isobaths during CODE-1. The larger observed decrease is consistent, however, with the speculation above that there is an increased drag at C1 due to the rock outcrops that were only present inshore of the 60-m isobath (Cacchione et al. 1983.)

5. Depth-dependent flow

a. *Comparison of model and observations*

The simple eddy viscosity model described in section 2c and the appendix is used to aid in interpreting the structure and dynamics of the depth-dependent portion of the flow. However, this simple model is only useful in this regard if it reproduces the basic vertical structure found in the observations. Consequently, this section begins with a comparison of the model results and the observations.

The same EOF analysis was applied to the model results as to the observations to facilitate comparison between the two. Prior to calculating the EOFs, the model output was decimated to 22 grid points roughly evenly spaced in the vertical because the logarithmic model grid has a disproportionate number of points near the boundaries, which would tend to weight the regions near the boundary more heavily than the interior in the EOF analysis. EOFs using only model results from the five depths of the current meters were similar to those using 22 vertical grid points, so the latter were used in the comparisons.

The largest EOF from the model results contains the depth-average alongshelf flow discussed in the previous section. However, it also includes some vertical structure similar to the vertical structure in the largest EOF from the observations (Fig. 10). As noted above (section 4) the model speeds are nearly twice as large as the observed speeds for this EOF. Comparison of the corresponding time series also reveals fairly good agreement aside from the amplitude of the response. (The largest EOF time series for both model and observations are nearly identical to the corresponding depth-averaged flow time series shown in Fig. 9.) Correlations between the largest EOF time series from the observations and the model results are 0.78–0.79, significant at the 99% confidence level (Bevington 1969), for the four different forms of the eddy viscosity profile.

Comparison of the vertical structures of the second EOFs also reveals good agreement between the observations and the model results (Fig. 11). Again, there

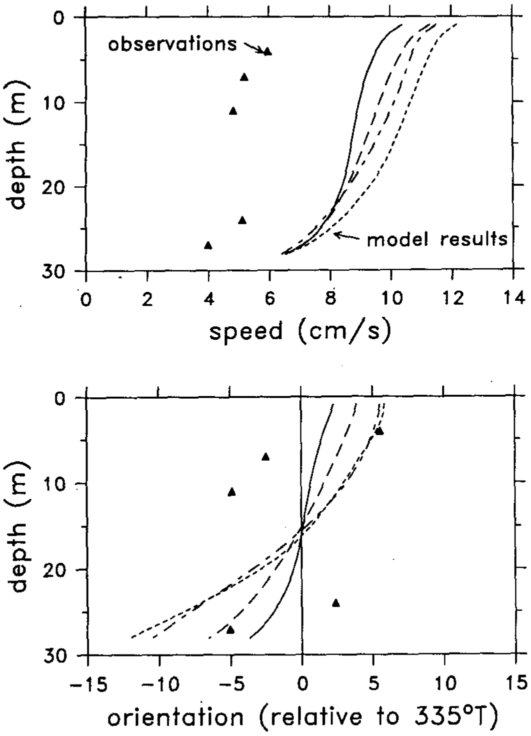

FIG. 10. Current speed (upper panel) and orientation (lower panel) profiles for the largest EOFs from the observations (△) and from the model results for bilinear (solid), cubic (long dash), bilinear cutoff (dash–dot), and exponential (short dash) eddy viscosity profiles.

is a discrepancy in the amplitude of the response with the observed response being larger than the model response in this case. However, model results from all four eddy viscosity profiles represent the essential vertical structure of the flow including the orientation of the flow, the change in orientation at about 10 m, and the relative amplitude of the near-surface and near-bottom flow. The corresponding time series from the model results are also in reasonable agreement with the second EOF time series from the observations (Fig. 12). Correlations range from 0.71 to 0.76, again significant at the 99% confidence level. (For convenience in comparing model and observations, the EOF time series are scaled by the square root of the modal variance divided by the number of stations.)

b. Interpretation of vertical structure

The comparisons indicate the model reproduces the basic temporal variability and vertical structure characterize by the largest two EOFs of the current observations. The model results also indicate that the vertical structure of the flow is not very sensitive to the structure of the eddy viscosity profile. These two results suggest that stratification may not play an important role in determining the vertical structure of the observed flow since there is no feedback between the mixing and the stratification in the simple eddy viscosity models considered.

While the largest EOF is dominated by the depth-averaged alongshelf flow, it also includes some vertical structure (Fig. 10). The model results indicate a slight (~10°) change in orientation with depth, with flow to the right of the interior flow near the surface and to the left near the bottom. In the model results the cross-shelf circulation near the bottom represents the bottom Ekman layer response to the bottom stress associated with the depth-averaged alongshelf flow. Comparison of the cross-isobath transport and the estimated bottom stress confirm this interpretation. This is reasonable since the bottom boundary-layer response will be strongly correlated with the depth-averaged alongshelf flow and will spin up on the same timescale and hence will tend to be incorporated in the same EOF. Because the depth-average cross-shelf velocity is zero, the upper-layer response is the corresponding return flow. While, the largest EOF from the observations has a similar vertical structure for speed, the observed orientations do not exhibit the structure seen in the model results, possibly because the orientation variations (~5°) are near the accuracy limits of the VMCM compasses.

The dominant vertical structure in the observations is contained in the second EOF, which exhibits flow in opposite directions in the upper and lower water

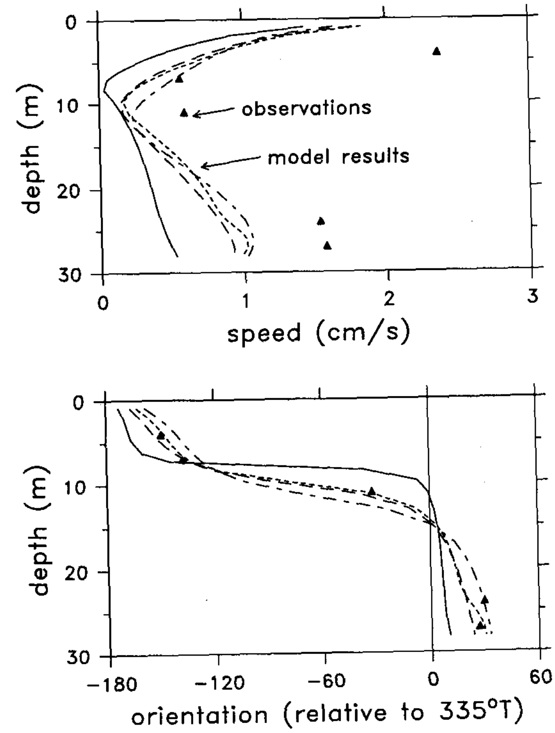

FIG. 11. Current speed (upper panel) and orientation (lower panel) profiles for the second EOFs from the observations (△) and from the model results for bilinear (solid), cubic (long dash), bilinear cutoff (dash–dot), and exponential (short dash) eddy viscosity profiles.

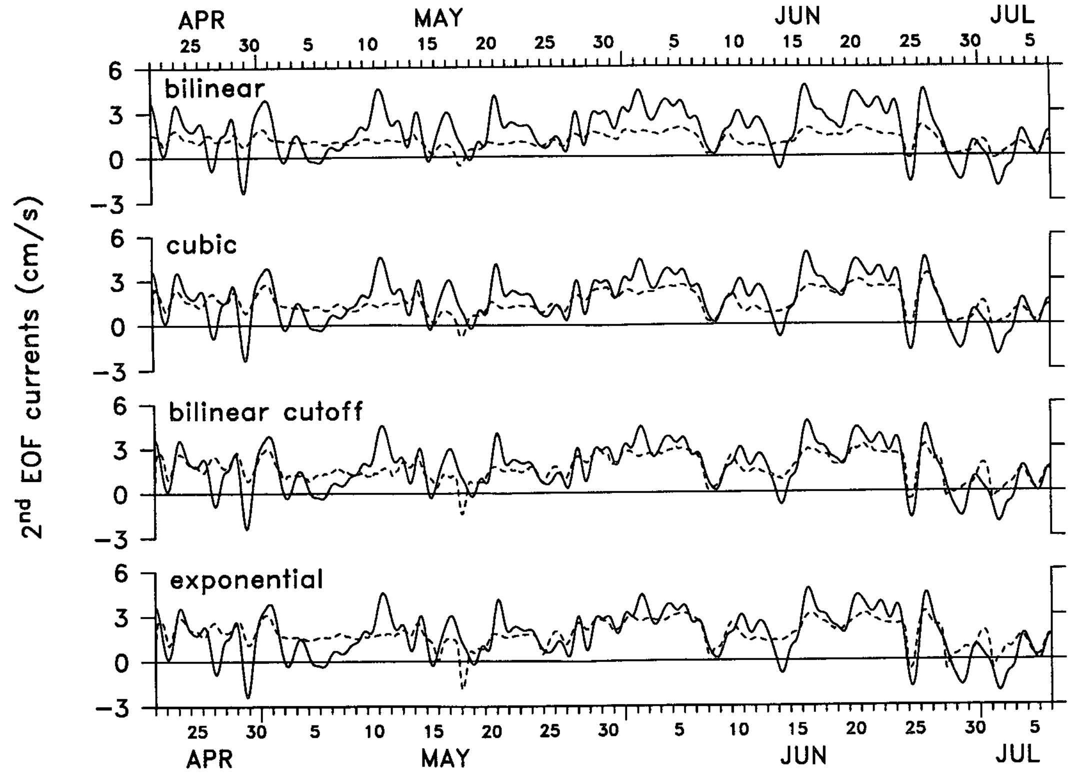

FIG. 12. Comparison of the time series for the second EOF from the observations and the model results for the four different eddy viscosity profiles. Correlations are between 0.71 and 0.76, significant at the 99% confidence level.

column with an orientation of about 30° relative to the depth-average flow and the local isobath orientation (Fig. 11). One explanation for the vertical structure and orientation of the second EOF is that it is a consequence of the shallowness of the water at the C1 site. However, model results for a water depth of 90 m did not yield a substantial change in the vertical structure of the second EOF, provided the relative magnitude of the wind stress and pressure gradient forcing remain the same. In particular, the near-surface and near-bottom flows were in opposite directions, oriented about 30° relative to local isobaths with the zero crossing at about 25 m (~30% of the water depth).

The model results indicate that the observed vertical structure is predominantly due to the character of the local forcing, with the wind stress opposed by an alongshelf pressure gradient, typically of similar magnitude. Thus, the equatorward wind stress tends to drive an equatorward and offshore flow near the surface while the opposing pressure gradient drives a poleward and onshore flow in the lower water column. To illustrate the influence of the two forcing terms on the vertical structure of the flow, average observed and modeled velocity, speed, and orientation profiles are shown in Fig. 13 for three periods: (a) 17–23 June when the wind stress and pressure gradient forcing are roughly equal (see Fig. 9); (b) 1–6 May when the wind stress is about three times larger than the pressure gradient forcing; and (c) 25–27 May when the pressure gradient forcing is about three times larger than the wind stress. To focus on the vertical structure of the flow the depth-averaged velocity has been removed in each case.

The flow has a different vertical structure during each of these periods. When the pressure gradient forcing dominates (25–27 May, Fig. 13c) there is a poleward flow with a maximum in the middle of the water column. The flow is onshore in the interior and offshore near the surface and bottom due to the wind and bottom stress, respectively. Consequently, there are zero crossings in the flow about 5 m below the surface and 5 m above the bottom. When the wind stress dominates (1–6 May, Fig. 13b) the vertical structure is antisymmetric about the center of the water column with equatorward and offshore flow in the upper half and poleward and onshore flow in the lower half of the water column. When the wind stress and pressure gradient forcing are about equal (17–23 June, Fig. 13a) there is one zero crossing, above the center of the water column, with stronger flow in the upper water column relative to the lower water column.

Some caution must be exercised in comparing the vertical structures in Fig. 13 to the vertical structure of the second EOF, since the former will include structure associated with the first EOF, as well as structure

a) June 17–23, 1981

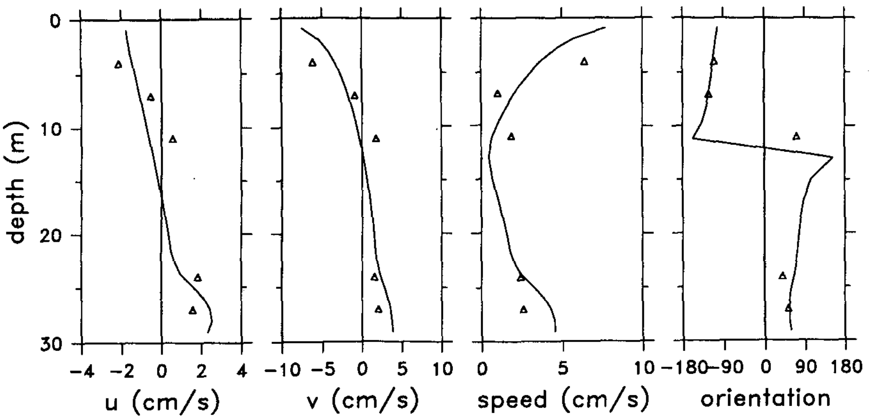

b) May 1–6, 1981

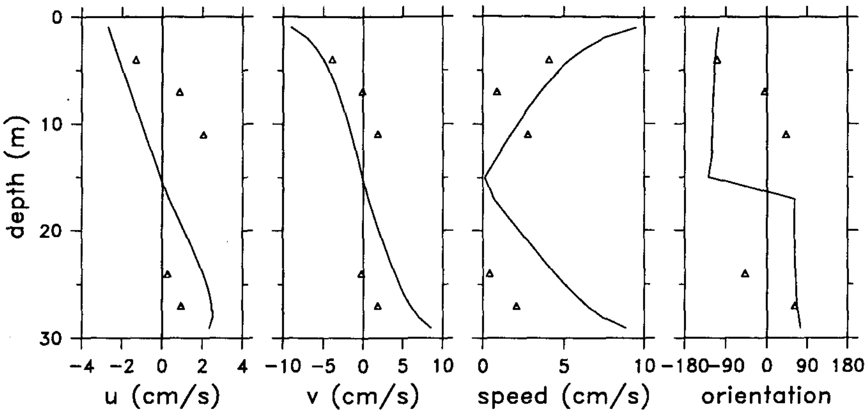

c) May 25–27, 1981

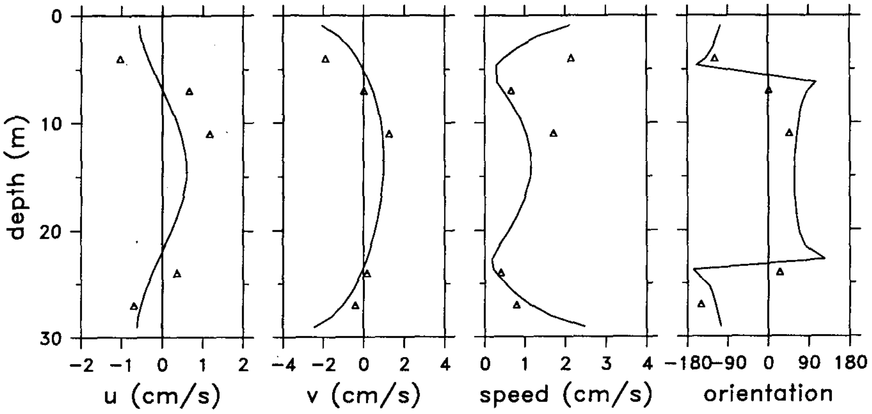

FIG. 13. Mean profiles of velocity (u and v), speed, and orientation from the observations (Δ) and model results for three periods: (a) 17–23 June when wind stress and pressure gradient forcing are about equal, −3.9 and −3.8 ($\times 10^{-4}$ cm s^{-2}), respectively; (b) 1–6 May when the wind stress is about three times larger than the pressure gradient forcing, −3.7 and −1.3 ($\times 10^{-4}$ cm s^{-2}), respectively; (c) 25–27 May when the wind stress is about one-third the pressure gradient forcing, −0.6 and −1.9 ($\times 10^{-4}$ cm s^{-2}), respectively. To facilitate comparison with the vertical structure of the second EOF (Fig. 11) the depth-average velocity has been removed from the profiles. The model results are for the exponential eddy viscosity profile. The other eddy viscosity profiles give similar results.

not contained in the first two EOFs. Nevertheless, the close agreement between the vertical structure of the second EOF and that in Fig. 13a suggests the observed vertical structure is primarily a consequence of the tendency for the alongshelf wind stress and pressure gradient to be about equal in magnitude and opposite in direction.

The dominant dynamical balance associated with the depth-dependent component of the model flow, and presumably the observed flow, is between the Coriolis and vertical stress divergence terms in (1). Accelerations are important in the alongshelf momentum balance but are fairly uniform with depth except very near the surface and bottom. Accelerations are insignificant in the cross-shelf momentum balance. The pressure gradient is assumed to be vertically uniform in both momentum balances. The vertical stress divergence is substantial throughout the water column, consistent with C1 being predominantly an inner-shelf site. In particular, at middepth the largest terms in the alongshelf momentum balance are the pressure gradient and the vertical stress divergence.

Another indication that C1 is within the inner shelf is provided by comparison of the observed cross-shelf transport (U_S) in the surface (or bottom) boundary layer to the deep water Ekman transport given by $\tau/(\rho_0 f)$. If C1 is within the inner shelf, then U_S should be less than $\tau/(\rho_0 f)$ because this is the region of cross-shelf divergence in the Ekman transport. The cross-shelf transport in the surface layer U_S was estimated by assuming the velocity at 4 m was uniform over a 10 m thick surface boundary layer. During times when there is a significant wind stress ($\tau^{Sy} > 0.2$ dyn cm^{-2} which is true about 80% of the time) U_S is typically about 25% of $\tau^{Sy}/(\rho_0 f)$ and never exceeds 85% of $\tau^{Sy}/(\rho_0 f)$, again suggesting that C1 is an inner-shelf location during the CODE-1 deployment.

For comparison, model runs were also made for the CODE-2 C2 mooring in 60 m of water. As noted in section 4a the depth-averaged alongshelf flow from the model agrees well with the observed depth-averaged flow at C2. However, the numerical model does not reproduce the vertical structure of the observed flow. In particular, the observed flow is more strongly sheared than the model flow. Time series associated with the second EOF from the model results are not significantly correlated with the second EOF from the observed C2 currents (maximum correlation 0.3). There is relatively strong and persistent stratification at C2 throughout both CODE-1 and CODE-2, with temperature differences of 1°–2°C across the water column (e.g., Winant et al. 1987). The neglect of this stratification probably accounts for the failure of the numerical model to reproduce the vertical structure of the currents at C2. (The depth-average flow dynamics are insensitive to the stratification.) The rock outcrops discussed above may contribute to the decrease in the stratification between C2 and C1. The presence of this persistent strong stratification suggests that the inner shelf may not have extented offshore to C2 during CODE-1 and CODE-2.

6. Summary

Analysis of current observations taken during CODE-1 in 30 m of water provides insight into the subtidal current dynamics at an inner-shelf site. The alongshelf flow is locally driven by both the wind stress and the alongshelf pressure gradient forcing. The wind stress and pressure gradient forcing have similar magnitudes but tend to oppose each other. The observed alongshelf currents are weaker than expected from simple two-dimensional model results or consideration of the depth-average alongshelf momentum balance (5), suggesting that the drag on the flow is larger than indicated by bottom tripod measurements made in the region. A likely source for the additional drag is large rock outcrops that are prevalent on the inner shelf in this region.

One of the more striking features of the C1 current observations is the weakness of the alongshelf current relative to flow at midshelf. Standard deviations of the depth-average alongshelf current are smaller by a factor of 4 at the inner-shelf C1 site relative to midshelf (C3). This decrease in the magnitude of the current variability is apparently due to a combination of at least three factors: a decrease in the wind stress toward the coast; the decrease in water depth resulting in a weaker body force due to the alongshelf pressure gradient; and the increased drag over the inner shelf.

The observed subtidal current variability exhibits a fairly simple and persistent vertical structure. At 4-m depth the flow tends to be offshore and equatorward. There is often a flow reversal at 7 to 11 m, with onshore and poleward flow in the lower two-thirds of the water column. The model results indicate that this vertical structure in the flow is primarily a consequence of the forcing; the equatorward wind stress tends to drive an equatorward and offshore flow near the surface, while the opposing alongshelf pressure gradient drives a poleward and onshore flow in the lower water column.

A simple, two-dimensional, eddy viscosity model reproduced most of the basic features of the observed flow, including its temporal variability, vertical structure, and orientation. The four eddy viscosity profiles considered gave similar results, suggesting that the basic characteristics of the C1 subtidal currents are not very sensitive to the form of the eddy viscosity profile. The success of the model in reproducing the quantitative features of the flow, particularly the vertical structure and orientation of the second EOF, supports the assumption that these features are not sensitive to variability in the weak stratification at the C1 site.

The observed offshore transport in the surface boundary layer (upper 10 m) is weaker than the deep water Ekman transport ($\tau^{Sy}/(\rho_0 f)$), and model results suggest that substantial vertical stress divergence extends throughout the water column. Both these results support the notion that C1 is an inner-shelf location where the surface and bottom boundary layers merge and there is a cross-shelf divergence in the Ekman transport.

The near-surface offshore transport and the corresponding onshore transport in the lower water column are roughly equal so that the depth-average cross-shelf velocity is small relative to the accuracy of the estimate on timescales of days to months. This is consistent with the circulation being two-dimensional. The agreement between the observations and the model results also supports the notion that the inner-shelf current dynamics at C1 are two-dimensional. The coastline and the inner-shelf isobaths in this region are not particularly straight over typical alongshelf displacement scales of $\sim$10 km or more (5 cm s^{-1} over a couple days) (Fig. 1), suggesting that inner-shelf dynamics may be two-dimensional even where the coastal topography is not simple. Because of the conceptual and theoretical simplifications associated with a two-dimensional characterization, this is an important and generally unresolved issue.

While this study provides a simple interpretation of the inner-shelf current dynamics at the C1 site off northern California, it is unclear what aspects are relevant to other inner-shelf locations. A number of studies suggest that (5) is a reasonable description of the depth-averaged alongshelf current over a variety of inner shelves (Pettigrew 1981; Lentz and Winant 1986; Masse 1988; and Lee et al. 1989). There are, however, very few inner-shelf observations resolving the vertical structure of the flow, particularly the cross-shelf circulation. The CODE-1 observations emphasize the difficulty of determining accurately the cross-shelf circulation over the inner-shelf. Not only is the flow weak relative to the accuracy of standard current meters but fairly dense vertical resolution is required. If, for example, the instrument at 4-m depth were not present, a completely different picture would have been drawn. More observational studies focusing on this region are needed if we are going to understand the role of the inner shelf in the overall shelf dynamics.

Acknowledgments. I thank all the CODE scientists whose efforts resulted in the high quality data that are the basis of this study. This work has benefited from discussions with J. Trowbridge, D. Chapman, and K. Brink, all at Woods Hole Oceanographic Institution, and thoughtful comments by C. Winant at Scripps Institution of Oceanography and an anonymous reviewer. This work was funded by the Ocean Sciences Division of the National Science Foundation under Grant OCE-9115713 and by the Office of Naval Research Coastal Science Program under Grant N00014-89-J-1074.

APPENDIX

Model Description

a. Model implementation

Equations (1)–(4) are solved numerically as in Lentz (1993) using a control volume approach (Patankar 1980). The model had 101 grid points in the vertical with logarithmically increasing grid spacing extending from both boundaries. A fully implicit time-stepping scheme is employed with a time step of one hour. Test runs indicate that both the vertical and temporal structure are well resolved with this grid. For simplicity, the initial velocity profile was zero throughout the water column. Because the frictional timescale is short (section 4a), this initial condition only has a noticeable influence on the solution over about 1 day. This is evident in the rapid ramp up from zero in the model time series shown in Figs. 9 and 12.

Since many of the eddy viscosity profiles considered depend on the bottom stress, which is not known a priori, an iterative scheme is required (e.g., Madsen 1977). To begin the iteration, an initial guess of the bottom stress is made based on the depth-average alongshelf momentum balance (5) assuming $|\tau^B| \approx |\tau^{By}|$. This estimate of the bottom stress is used to determine the eddy viscosity profile and (1) is solved for $\mathbf{v}(z)$. The resulting velocity profile is then used to estimate a new bottom stress that is in turn used to determine a new eddy viscosity profile. This procedure generally converges rapidly, in a few iterations, and is stopped when the change in the bottom shear velocity ($u_*^B = |\tau^B/\rho_0|^{1/2}$) is less than 10^{-4} m s^{-1}.

An iterative scheme is also used to find the value of $\partial P/\partial x$ that satisfies (4). An initial guess is made, again based on (5), and the resulting velocity profile is used to estimate U. Subsequent estimates of $\partial P/\partial x$ to minimize U are found using a linear search procedure. In most cases a $\partial P/\partial x$ that yields an fU less than a few percent of the terms in (5) is achieved in 5–10 iterations. Jenter and Madsen (1989) use a similar procedure in their study of bottom stress for wind-driven depth-average flows.

The model is forced with the low-pass filtered time series of τ^S and $\partial P/\partial y$ shown in Fig. 9. Because (1) is nonlinear due to the dependence of A_v on u_*^B, it may not be appropriate to force the model with low-pass filtered time series. In particular, tides and other higher frequency motions may contribute to the bottom stress and hence to the drag on the subinertial flow. The influence of including higher frequency motions is examined in section 4b.

b. Eddy viscosity profiles

Four forms of the eddy viscosity profile are considered (Fig. A1): a bilinear profile (Madsen, 1977); a bilinear cutoff profile (Deardorff 1972; Smith and Long

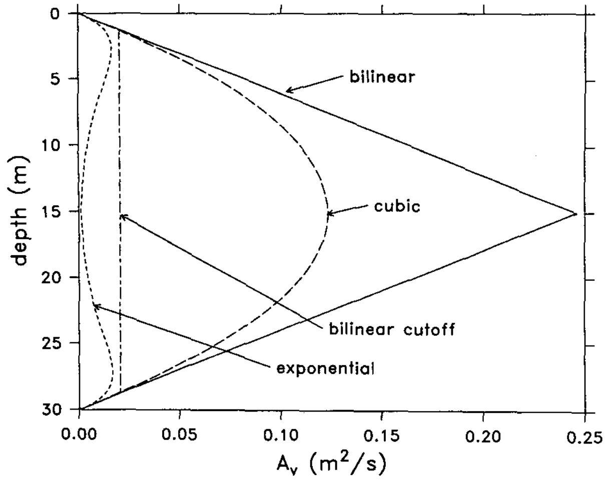

FIG. A1. Examples of the four types of eddy viscosity profiles considered. In general, the magnitude of the eddy viscosity depends on the surface and bottom stresses, and the profiles are not symmetric unless the surface and bottom stresses happen to be equal.

1976); a cubic profile (Signell et al. 1990); and a bilinear one that decays exponentially toward zero in the interior (Long 1981; Glenn 1983). All these eddy viscosity profiles have the form $A_v = \kappa u_* z'$ near the boundaries, where $\kappa = 0.4$ is von Kármán's constant and z' is distance from the boundary. They differ in how they extend into the interior of the fluid. A constant eddy viscosity profile was not considered, because there is considerable evidence that a constant eddy viscosity profile is not appropriate for oceanic flows (see the discussion in Lentz 1993), and it is unclear a priori what value to choose for a constant eddy viscosity. The various forms of the eddy viscosity profile considered are discussed in detail in Lentz (1993). A brief description is given below.

The bilinear profile suggested by Madsen (1977) extends the linear profiles into the interior. The vertical extent of the linear portions associated with the surface and bottom stresses are weighted by their respective u_* so that the stronger stress influences more of the water column. This generally leads to a discontinuity in the eddy viscosity profile at the matching depth (Jenter and Madsen 1989).

The cubic profile is the simplest polynomial that can match the two constraints at each boundary: that the eddy viscosity approach zero and the slope be κu_* (Signell et al. 1990), where u_* will in general be different at the surface and bottom boundaries.

The bilinear cutoff profile is linear near the boundaries and constant in the interior. The distance from the boundary beyond which the eddy viscosity is constant is chosen to be 10% of the turbulent boundary-layer scale δ (e.g., Smith and Long 1976) (where $\delta = \kappa u_*/f$). Since the surface and bottom boundary cutoff values for the eddy viscosity are not generally the same, they are joined by a linear interior profile.

The exponential profile is similar to the bilinear cutoff profile except that away from the boundary the eddy viscosity decays exponentially toward zero; that is, $A_v(z') = \kappa u_* z' \exp(-z'/l)$ (Long 1981; Glenn 1983), where l is the exponential decay scale, which was somewhat arbitrarily chosen to be 0.27δ. For this choice the eddy viscosity decays to about 1% of its maximum value at a distance of 2δ from the boundary in deep water. This eddy viscosity profile is qualitatively similar to the profiles from more sophisticated turbulence closure models (e.g., Weatherly and Martin 1978).

For the bilinear cutoff and exponential profiles a cutoff elevation or exponential decay scale must be prescribed. While Lentz (1993) has pointed out that the cross-shelf circulation on the inner-shelf is sensitive to the choice of these parameters, no attempt is made to adjust these parameters to fit the data. Consequently, in the model runs there are no adjusted parameters in prescribing the eddy viscosity profiles.

REFERENCES

Allen, J. S., R. C. Beardsley, J. O. Blanton, W. C. Biocourt, B. Butman, L. K. Coachman, A. Huyer, T. H. Kinder, T. C. Royer, J. D. Schumacher, R. L. Smith, and W. Sturges, 1983: Physical oceanography of continental shelves. *Rev. of Geophys. Space Phys.* **21**(5), 1149–1181.

Bevington, P. R., 1969: *Data Reduction and Error Analysis for the Physical Sciences.* McGraw-Hill, 336 pp.

Brown, W. S., J. D. Irish, and C. D. Winant, 1987: A description of subtidal pressure field observations on the northern California shelf during the Coastal Ocean Dynamics Experiment. *J. Geophys. Res.*, **92**(C2), 1605–1636.

Cacchione, D. A., D. E. Drake, W. D. Grant, A. J. Williams, and G. B. Tate, 1983: Variability of sea-floor roughness within the Coastal Ocean Dynamics Experiment (CODE) region. Woods Hole Oceanographic Institution Tech. Rep. WHOI-83-25, 44 pp.

Davis, R. E., 1976: Predictability of sea surface temperature and sea level pressure anomalies over the North Pacific Ocean. *J. Phys. Oceanogr.*, **6**, 249–266.

Deardorff, J. W., 1972: Numerical investigation of neutral and unstable planetary boundary layers. *J. Atmos. Sci.*, **29**, 91–115.

Drake, D. E., D. A. Cacchione, and W. D. Grant, 1992: Shear stress and bed roughness estimates for combined wave and current flows over a rippled bed. *J. Geophys. Res.*, **97**(C2), 2319–2326.

Ekman, V. W., 1905: On the influence of the earth's rotation on ocean currents. *Ark. Mat. Aston. Fys.*, **2**(11), 1–53.

Glenn, S. M., 1983: A continental shelf bottom boundary layer model: The effects of waves, currents and moveable bed. Ph.D. thesis, Woods Hole Oceanographic Institution/Massachusetts Institute of Technology, 237 pp.

Grant, W. D., A. J. Williams, and S. M. Glenn, 1984: Bottom stress estimates and their prediction on the northern California continental shelf during CODE-1: The importance of wave–current interaction. *J. Phys. Oceanogr.*, **14**, 506–527.

Hickey, B. M., and N. E. Pola, 1983: The seasonal alongshore pressure gradient on the west coast of the United States. *J. Geophys. Res.*, **88**(C12), 7623–7633.

Jenter, H. L., and O. S. Madsen, 1989: Bottom stress in wind-driven depth-averaged coastal flow. *J. Phys. Oceanogr.*, **19**(7), 962–974.

Kosro, P. M., 1987: Structure of the coastal current field off northern California during the Coastal Ocean Dynamics Experiment. *J. Geophys. Res.*, **92**(C2), 1637–1654.

Large, W. G., and S. Pond, 1981: Open ocean momentum flux measurements in moderate to strong winds. *J. Phys. Oceanogr.*, **11**, 324–336.

Lee, T. N., E. Williams, R. Evans, J. Wang, and L. Atkinson, 1989: Response of South Carolina continental shelf waters to wind and gulf stream forcing during winter of 1986. *J. Geophys. Res.*, **94**(C8), 10 715–10 754.

Lentz, S. J., 1990: CODE (Coastal Ocean Dynamics Experiment): A Collection of Reprints. Woods Hole Oceanographic Institution, 817 pp.

——, 1993: Sensitivity of the inner-shelf circulation to the form of the eddy-viscosity profile. *J. Phys. Oceanogr.*, in press.

——, and C. D. Winant, 1986: Subinertial currents on the southern California shelf. *J. Phys. Oceanogr.*, **16**, 1737–1750.

——, and D. C. Chapman, 1989: Seasonal differences in the current and temperature variability over the northern California shelf during the Coastal Ocean Dynamics Experiment. *J. Geophys. Res.*, **94**(C9), 12 571–12 592.

Long, C. E., 1981: A simple model for time-dependent stably stratified turbulent boundary layers. Tech. Rep. Special Report No. 95, University of Washington, Seattle, WA, 170 pp.

Madsen, O. S., 1977: A realistic model of the wind-induced Ekman boundary layer. *J. Phys. Oceanogr.*, **7**, 248–255.

Masse, A. K., 1988: Estuary-shelf interaction: Delaware Bay and the inner-shelf. Ph.D. thesis, University of Delaware, 216 pp.

Mitchum, G. T., and A. J. Clarke, 1986: The frictional nearshore response to forcing by synoptic scale winds. *J. Phys. Oceanogr.*, **16**, 934–946.

Patankar, S. V., 1980: *Numerical Heat Transfer and Fluid Flow.* Hemisphere Publishing, 197 pp.

Pettigrew, N. R., 1981: The dynamics and kinematics of the coastal boundary layer off Long Island. Ph.D. thesis, Woods Hole Oceanographic Institution, 262 pp.

Rosenfeld, L. K., 1983: CODE-1: Moored array and large-scale data report. Woods Hole Oceanographic Institution Tech. Rep. WHOI-83-23, 186 pp.

Samelson, R. M., 1992: Supercritical marine layer flow along a smoothly varying coastline. *J. Atmos. Sci.*, **49**(17), 1571–1584.

Schlichting, H., 1979: *Boundary Layer Theory.* 7th ed. McGraw-Hill, 817 pp.

Send, U., R. C. Beardsley, and C. D. Winant, 1987: Relaxation from upwelling in CODE. *J. Geophys. Res.*, **92**(C2), 1683–1698.

Signell, R. P., R. C. Beardsley, H. C. Graber, and A. Capotondi, 1990: Effect of wave-current interaction on wind-driven circulation in narrow, shallow embayments. *J. Geophys. Res.*, **95**(C6), 9671–9678.

Smith, R. L., 1981: A comparison of the structure and variability of the flow field in three coastal upwelling regions: Oregon, Northwest Africa, and Peru. *Coastal Upwelling,* F. A. Richards, Ed., Amer. Geophys. Union, 107–118.

——, and C. E. Long, 1976: The effect of turning in the bottom boundary layer on continental shelf sediment transport. *Mem. Soc. Roy. Sci. Liege, Ser.*, **6**, 369–396.

——, and S. R. McClean, 1977: Spatially averaged flow over a wavy surface. *J. Geophys. Res.*, **82**, 1735–1746.

Weatherly, G. L., and P. J. Martin, 1978: On the structure and dynamics of the oceanic bottom boundary layer. *J. Phys. Oceanogr.*, **8**, 557–570.

Weller, R. A., and R. E. Davis, 1980: A vector-measuring current meter. *Deep-Sea Res.*, **27**, 575–582.

Winant, C. D., R. C. Beardsley, and R. E. Davis, 1987: Moored wind, temperature and current observations made during CODE-1 and CODE-2 over the northern California continental shelf and upper slope. *J. Geophys. Res.*, **92**(C2), 1569–1604.

——, C. Dorman, C. Friehe, and R. Beardsley, 1988: The marine layer off northern California: An example of supercritical channel flow. *J. Atmos. Sci.*, **45**(23), 3588–3605.